energies

MDPI

Article

[NiFe]-(Oxy)Sulfides Derived from $NiFe_2O_4$ for the Alkaline Hydrogen Evolution Reaction

David Tetzlaff [1,2], Vasanth Alagarasan [2], Christopher Simon [3], Daniel Siegmund [1,2], Kai junge Puring [1], Roland Marschall [3] and Ulf-Peter Apfel [1,2,*]

[1] Fraunhofer Institute for Environmental, Safety and Energy Technology UMSICHT, 46047 Oberhausen, Germany; david.tetzlaff@umsicht.fraunhofer.de (D.T.); daniel.siegmund@umsicht.fraunhofer.de (D.S.); kai.junge.puring@umsicht.fraunhofer.de (K.j.P.)
[2] Inorganic Chemistry I, Ruhr University Bochum, 44780 Bochum, Germany; Vasanth.Alagarasan@ruhr-uni-bochum.de
[3] Physical Chemistry III, University of Bayreuth, 95447 Bayreuth, Germany; Christopher.Simon@uni-bayreuth.de (C.S.); Roland.Marschall@uni-bayreuth.de (R.M.)
* Correspondence: ulf.apfel@rub.de or ulf-peter.apfel@umsicht.fraunhofer.de

Abstract: The development of noble-metal-free electrocatalysts is regarded as a key factor for realizing industrial-scale hydrogen production powered by renewable energy sources. Inspired by nature, which uses Fe- and Ni-containing enzymes for efficient hydrogen generation, Fe/Ni-containing chalcogenides, such as oxides and sulfides, received increasing attention as promising electrocatalysts to produce hydrogen. We herein present a novel synthetic procedure for mixed Fe/Ni (oxy)sulfide materials by the controlled (partial) sulfidation of $NiFe_2O_4$ (NFO) nanoparticles in H_2S-containing atmospheres. The variation in H_2S concentration and the temperature allows for a precise control of stoichiometry and phase composition. The obtained sulfidized materials (NFS) catalyze the hydrogen evolution reaction (HER) with increased activity in comparison to NFO, up to −10 and −100 mA cm^{-2} at an overpotential of approx. 250 and 450 mV, respectively.

Keywords: hydrogen; oxysulfide; electrocatalysis; alkaline hydrogen evolution reaction

check for updates

Citation: Tetzlaff, D.; Alagarasan, V.; Simon, C.; Siegmund, D.; junge Puring, K.; Marschall, R.; Apfel, U.-P. [NiFe]-(Oxy)Sulfides Derived from $NiFe_2O_4$ for the Alkaline Hydrogen Evolution Reaction. *Energies* **2022**, *15*, 543. https://doi.org/10.3390/en15020543

Academic Editor: Johannes Schaffert

Received: 29 November 2021
Accepted: 10 January 2022
Published: 13 January 2022

1. Introduction

The electrochemical hydrogen evolution reaction (HER) is a promising approach to foster hydrogen usage for replacing fossil fuels as major energy carriers [1,2]. Currently, electrocatalysts based on noble metals such as Pt are primarily used as cathode material in electrolyzers due to their outstanding performance; however, the scarcity of common noble metals impedes widespread application [3–5]. Therefore, scientists have focused on earth-abundant transition metal chalcogenides such as oxides and sulfides as cost-effective alternatives to Pt for the HER [6–8]. Transition metal oxides are characterized by their compositional and structural flexibility, which offer a high diversity in the electronic and crystal structure. Although transition metal oxides are regarded as catalytically inert for the HER, defect engineering or the introduction of dopants enabled an improved HER performance [9–11]. In contrast, transition metal sulfides can overcome the major drawbacks of metal oxides such as poor electronic conductivity, unsuitable hydrogen adsorption and limited catalytic-active sites [12–14]. To combine the properties of transition metal oxides and sulfides, researchers have focused on the synthesis of distinct transition metal oxysulfides, which contain oxygen and sulfur. Commonly, the synthesis of oxysulfides can be achieved by multiple pathways, including the sulfidation of an oxygenated phase, the oxidation of sulfides, the reduction of sulfates or by the co-insertion of oxygen and sulfur [15]. In this respect, Nelson et al. synthesized CoO_xS_y hollow nanoparticles by substituting oxide with sulfide species in CoO using ammonium sulfide in oleylamine at 100 °C [16]. The obtained electrocatalysts displayed sulfur-content-dependent HER activity,

with the highest activity for $CoO_xS_{0.18}$. Another oxysulfide material was synthesized by Sarma et al. by the anodic oxidation of WS_2 sheets [17]. Here, distinct WO_xS_y materials were obtained depending on the deposition potential, which has shown the highest HER performance for the WO_xS_y material, which was deposited at 5 V.

In terms of hydrogen production, nature has established Fe- and Ni-containing enzymes (hydrogenases), which effectively perform the reversible conversion of hydrogen to protons and electrons [18–20]. Inspired by the natural evolutionary choice of transition metals, numerous Fe/Ni-containing catalysts were synthesized, which showed high catalytic activities for the HER [21–27]. Furthermore, Fe/Ni oxysulfide materials were synthesized displaying promising activities towards the HER and oxygen evolution reaction (OER) [28,29]. However, investigating the HER activity of Fe/Ni oxysulfides with different sulfur to metal (S:M) ratios and material phases has not yet been realized.

In lieu, we herein present the synthesis of various NiFe (oxy)sulfide materials by the sulfidation of $NiFe_2O_4$ with H_2S. We demonstrate a controlled sulfidation towards a nickel containing pyrite and pyrrhotite depending on the H_2S gas composition as well as on the temperature. Finally, we show the performance of the synthesized NiFe (oxy)sulfide materials towards the HER in an alkaline medium.

2. Materials and Methods

2.1. Chemicals

The sulfidizing gases H_2S/N_2 (50:50) and H_2S/H_2 (15:85) (Air Products, Hattingen, Germany), as well as KOH (Fisher Scientific, Dreieich, Germany, >85%), were purchased from commercial vendors and used without further purification.

2.2. Synthesis of Sulfidized $NiFe_2O_4$ (NFS) Materials

The synthesis of the starting material $NiFe_2O_4$ was realized according to protocols recently published in the literature [30]. For subsequent sulfidation reactions, 100 mg of $NiFe_2O_4$ was placed into a tubular furnace and purged for 10 min with H_2S/N_2 (50:50) or H_2S/N_2 (15:85). Maintaining the gas flow, the furnace was heated to $100 \leq T \leq 300$ °C and the temperature was held for 1 h. The furnace was then allowed to cool down to room temperature within approx. 20 min using pressurized air while applying a N_2 gas flow.

2.3. Characterization

2.3.1. Physical Characterization

Characterization of the investigated materials was performed by powder X-ray diffraction (PXRD) using a HUBER powder X-ray diffractometer (HUBER, Rimsting, Germany) equipped with a Mo-K_α source. The 2-Θ values were converted to values from a Cu-K_α, according to Bragg's law of diffraction.

The particle sizes of the synthesized electrocatalysts were determined using a SALD-2300 laser diffraction particle size analyzer (Shimadzu, Duisburg, Germany) equipped with a SALD-BC23 batch cell. The respective samples were prepared by dispersing approx. 10 mg of the catalyst material for 1 min in 1 mL isopropyl alcohol using an ultra-sonic bath. Subsequently, a portion of the dispersion was added to the batch cell, which was filled with isopropyl alcohol. The obtained particle sizes were calculated using the Fraunhofer approximation and the volume was chosen based on the dimensions of the particle amount.

A Gemini2 Merlin HR-FESEM (ZEISS, Oberkochen, Germany) was used for scanning electron microscopy (SEM), equipped with an OXFORD AZtecEnergy X-ray microanalysis system for energy dispersive X-ray spectroscopy (EDX). Samples were dispersed in 1 mL isopropyl alcohol and ultra-sonicated for 1 min. Afterwards, the samples were drop-casted on a flat Si Wafer for analysis. The SEM images were recorded at an acceleration voltage of 5 kV while EDX mappings were performed from 0–20 kV.

X-ray photoelectron spectroscopy (XPS) measurements were performed with a polychromatic Al-K_α X-ray source (anode operating at 14 kV and 13 mA) combined with an ultra−High-vacuum (UHV, 10^{-9} mbar) setup and a hemispherical analyzer (type CLAM2,

VG, Scientific, Thermo Fisher Scientific, Dreieich, Germany). A pass energy of 100 eV was applied to record the spectra.

2.3.2. Electrochemical Characterization

The (oxy)sulfide electrocatalysts were investigated as drop-casted materials on a glassy carbon (GC) rod electrode. For this purpose, 11.78 mg of the catalyst material was dispersed in a mixture composed of 0.30 mL water, 0.15 mL isopropanol and 0.05 mL Nafion (5 % in aliphatic alcohols) using an ultra-sonic bath for 30 min. Subsequently, 3 µL of the catalyst ink was applied on a GC electrode (d = 3 mm, 1 mg cm^{-2} catalyst), which was dried at room temperature for 30 min. Before drop-casting, the GC electrode was polished using Al_2O_3 pastes with grain sizes of 0.30 and 0.05 µm for 3 min, each followed by ultra-sonication in Milli-Q water for 5 min.

Electrochemical measurements were performed in a three-electrode setup, employing the catalyst-modified GC working electrode (WE), a Pt mesh counter electrode (CE) and a Hg/HgO (1 M KOH) reference electrode (RE) in 1 M KOH. The WE and CE were separated by utilizing an H-type electrolysis cell with both half-cells being separated by an anion exchange separator (Zirfon®, AGFA, Mortsel, The Netherlands). Electrochemical measurements were conducted using a GAMRY Reference 600 or Reference 600 + (C3-Analysentechnik, Haar, Germany) and the measured potentials were converted to the reversible hydrogen electrode (RHE) reference according to the equation: $E_{RHE} = E_{measured} + E_{Ref.} + 0.059$ pH.

For the HER experiments, the material was first electrochemically conditioned through cyclic voltammetry (CV) between 0 and −0.3 V vs. RHE at 100 mV s^{-1} until a stable voltammogram was obtained. The investigation of the electrochemical surface area (ECSA) was realized through CV measurements between −0.16 and −0.24 V vs. RHE at scan rates of 40, 80, 120, 160 and 200 mV s^{-1}, respectively. Changes in the electrochemical activity were monitored via linear sweep voltammetry (LSV) between 0 and −0.45 V vs. RHE at a scan rate of 1 mV s^{-1}. Electrochemical impedance spectroscopy (EIS) measurements were conducted at −0.4 V vs. RHE from 100 kHz to 0.10 Hz taking 7 points per decade at an amplitude of 7 mV rms. Stability tests were performed using chronopotentiometry at −10 or −100 mA cm^{-2} for at least one hour.

3. Results and Discussion

3.1. Synthesis and Physical Characterization

The synthesis of NiFe-(oxy)sulfides (NFS) was performed by utilizing $NiFe_2O_4$ (NFO) as the starting compound. The NFO precursor was treated with different H_2S gas compositions (H_2S/N_2, (50:50) and H_2S/H_2 (15:85)) at different temperatures ($100 \leq T \leq 300$ °C) to control the sulfur to metal (S:M) ratio in the materials [31]. For clarity, the synthesized materials are referred to as NFS_T-N_2 and NFS_T-H_2, where T represents the temperature in °C and N_2 and H_2 the diluting gases.

The obtained materials were analyzed by powder X-ray diffraction (PXRD) and show distinct phase formations depending on the applied temperature and H_2S gas composition (Figure 1). Treatment of $NiFe_2O_4$ in either the H_2S/N_2 or H_2S/H_2 gas mixture results in no visible change in the powder pattern compared to NFO when heated below 200 °C, indicating a conservation of the NFO phase. Starting at 200 °C, phase transformations occur, which become more prominent at higher temperatures. Using a H_2S/N_2 atmosphere, phase transformations towards nickelian pyrite ($Ni_{0.35}Fe_{0.65}S_2$) were observed, while the usage of H_2S/H_2 resulted in phase transformations towards nickelian pyrrhotite ($Ni_{0.35}Fe_{0.65}S$). Notably, the crystallinity of the synthesized materials increases with temperature and no further phase transformation occurred after heating the samples for longer than 1 h.

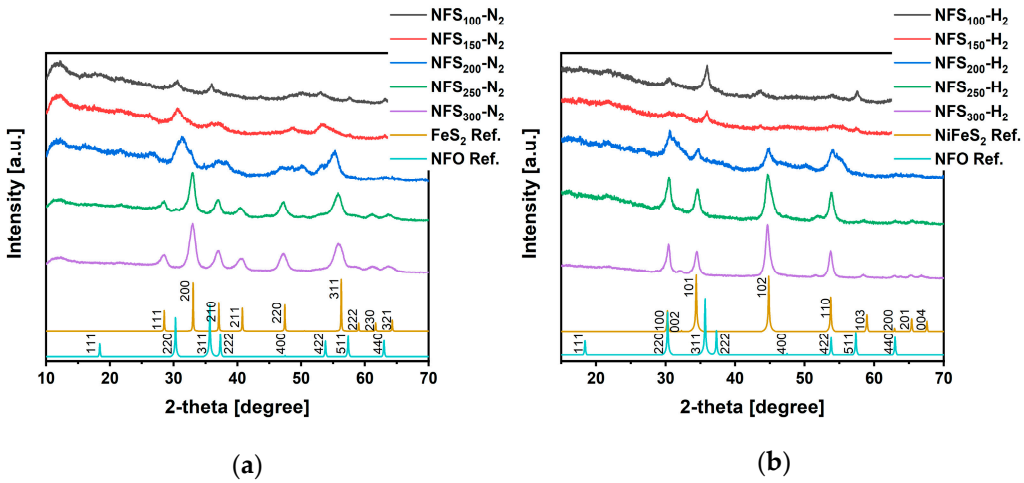

(**a**) (**b**)

Figure 1. Powder X-ray diffractograms of NFS materials synthesized at temperatures between 100 and 300 °C using (**a**) H_2S/N_2 and (**b**) H_2S/H_2 reaction atmospheres [32–34].

To further clarify the composition of the obtained NFS materials, X-ray photoelectron spectroscopy (XPS) measurements were performed (Figure S1 in Supplementary Materials). The XPS spectra show characteristic peaks of the two $p_{3/2}$ orbitals of Ni and Fe at approx. 858 and 710 eV, respectively. Furthermore, all materials show a peak in the O 1s spectrum at approx. 532 eV, which can be ascribed to either metal–oxygen bonds, low-coordinated oxygen ions at the surface or adsorbed water [29]. Interestingly, the XPS analysis reveals the presence of sulfur in each NFS sample, which indicates a sulfidation of NFO below 200 °C.

In order to quantify the S:M ratios, the synthesized materials were subjected to energy dispersive spectroscopy (EDX) (Table 1). While no phase changes in the powder patterns are observable, sulfur was detected in the $NFS_{100}-N_2$ and $NFS_{100}-H_2$ materials with S:M ratios of 1.09 ± 0.09 and 0.79 ± 0.26, respectively. For $NFS-N_2$, the S:M ratio undergoes a slight increase until 250 °C (S:M ratio = 1.49 ± 0.06) and a much steeper increase up to 300 °C with a S:M ratio of 1.98 ± 0.26. For the $NFS-H_2$ materials, the S:M ratio increases until reaching a S:M ratio of 1.20 ± 0.08 for $NFS_{200}-H_2$, which subsequently decreases to a S:M ratio of 1.15 ± 0.06 for $NFS_{300}-H_2$. According to the EDX analysis, the sum formulas of the nickelian pyrite and pyrrhotite were calculated to $Ni_{0.30}Fe_{0.71}S_{1.99}$ and $Ni_{0.30}Fe_{0.64}S_{1.06}$, at that point reaching complete sulfidation. Thus, the obtainable phases (NFO, nickelian pyrite or pyrrhotite) as well as the degree of sulfidation can be controlled by the variation of S-source gas composition and temperature.

Table 1. Energy-dispersive X-ray emission (EDX) analysis of the investigated electrocatalysts displaying the obtained Fe:Ni and the S:M ratio.

Material	Fe:Ni Ratio	S:M Ratio	Sum Formula
NFO	2.46 ± 0.10	0	$Ni_{0.30}Fe_{0.74}O_x$
$NFS_{100}-N_2$	1.93 ± 0.96	1.09 ± 0.09	$Ni_{0.3}Fe_{0.52}S_{0.87}O_x$
$NFS_{150}-N_2$	2.47 ± 0.30	1.29 ± 0.22	$Ni_{0.3}Fe_{0.74}S_{1.29}O_x$
$NFS_{200}-N_2$	2.18 ± 0.41	1.34 ± 0.10	$Ni_{0.3}Fe_{0.64}S_{1.26}O_x$
$NFS_{250}-N_2$	2.50 ± 0.33	1.49 ± 0.06	$Ni_{0.3}Fe_{0.74}S_{1.54}O_x$
$NFS_{300}-N_2$	2.33 ± 0.31	1.98 ± 0.26	$Ni_{0.3}Fe_{0.71}S_{1.99}$
$NFS_{100}-H_2$	2.43 ± 0.49	0.79 ± 0.26	$Ni_{0.3}Fe_{0.71}S_{0.80}O_x$
$NFS_{150}-H_2$	2.58 ± 0.45	1.09 ± 0.34	$Ni_{0.3}Fe_{0.76}S_{1.14}O_x$
$NFS_{200}-H_2$	2.41 ± 0.33	1.20 ± 0.08	$Ni_{0.3}Fe_{0.71}S_{1.21}O_x$
$NFS_{250}-H_2$	2.35 ± 0.37	1.11 ± 0.15	$Ni_{0.3}Fe_{0.70}S_{1.04}O_x$
$NFS_{300}-H_2$	2.18 ± 0.31	1.15 ± 0.06	$Ni_{0.3}Fe_{0.64}S_{1.07}$

Scanning electron microscopy (SEM) characterization of the obtained materials reveals comparable particle morphologies and sizes for all tested samples (Figures S2 and S3). In general, spherical shaped particles with sizes in the nanometer range are present, which form larger agglomerates with a rough surface morphology. A more detailed picture of the size distribution of the obtained NFS materials is given by laser diffraction analysis (Figure S4). In general, all materials display a broad particle size distribution. For example, the NFO precursor shows a significant number of particles in the nanometer range as well as in the micrometer range (up to 100 µm). In comparison, the particle size distribution of the NFS materials shows a shift towards larger particles of up to 400 µm, indicating agglomeration. However, a correlation of the particle sizes with the applied temperature cannot be observed and for obtaining smaller particle sizes post-synthetic milling is suggested.

3.2. Electrochemical Hydrogen Evolution Reaction

To further investigate the dependence of the alkaline HER activity on the S:M ratio of the synthesized NFS compounds and to observe trends arising from this alteration, electrodes were prepared via drop-casting and served as working electrodes in a three-electrode setup employing an H-type electrolysis cell.

For a first analysis, the electrochemical activity was determined by linear sweep voltammetry (LSV) at a scan rate of 1 mV s^{-1} (Figure 2a,d). The investigated electrocatalytic materials display distinct overpotentials vs. RHE at a current density of −10 mA cm^{-2} depending on the catalyst composition. For instance, the usage of the NFO precursor as an HER catalyst resulted in almost no catalytic activity. In contrast, all sulfidized materials show a lower overpotential compared to NFO. Using the NFS−N_2 electrocatalysts, the lowest overpotential at −10 mA cm^{-2} was observed for $NFS_{100}-N_2$ at 266 ± 12 mV. The overpotential increases for catalysts synthesized at higher temperatures up to 394 ± 24 mV for $NFS_{250}-N_2$. Surprisingly, the $NFS_{300}-N_2$ electrocatalyst displays an increased catalytic activity in contrast to $NFS_{250}-N_2$ with an overpotential of 346 ± 4 mV. In comparison, the highest HER activity for the NFS−H_2 electrocatalysts was observed for $NFS_{250}-H_2$ with an overpotential of 302 ± 9 mV, which increases to 408 ± 30 mV for $NFS_{150}-H_2$. Notably, the lowest overpotentials are observed for NFS−N_2 electrocatalysts synthesized at temperatures around 100 °C and for NFS−H_2 electrocatalysts synthesized around 250 °C, which show a S:M ratio of approx. 1:1. However, since most of the NFS−H_2 electrocatalysts display similar S:M ratios, the presence of the nickelian pyrrhotite phase seems to play a major role for increased HER activity.

To test this theory, we normalized the LSV curves by the electrochemical surface area (ECSA) to exclude particle size effects from the electrochemical activity. For this purpose, the ECSA was determined by measuring the double layer capacitance (C_{DL}) of the materials using cyclic voltammetry (Figure 2b,e). The NFS−N_2 electrocatalysts display similar C_{DL} values, with $NFS_{150}-N_2$ having the highest C_{DL} of 51 ± 6 mF cm^{-2}, followed by $NFS_{250}-N_2$ (49 ± 2 mF cm^{-2}), $NFS_{200}-N_2$ (45 ± 5 mF cm^{-2}) and $NFS_{100}-N_2$ (44 ± 3 mF cm^{-2}). Interestingly, the $NFS_{300}-N_2$ electrocatalyst displays a C_{DL} of 11 ± 1 mF cm^{-2}, which is several times lower than the other NFS−N_2 electrocatalysts. The NFS−H_2 electrocatalysts display the highest C_{DL} for $NFS_{100}-H_2$ (44 ± 3 mF cm^{-2}) and $NFS_{150}-H_2$ (51 ± 6 mF cm^{-2}), which decreases with increasing temperature during the synthesis down to 12 ± 2 mF cm^{-2} for $NFS_{300}-H_2$. The calculation of the ECSA was performed by dividing the obtained C_{DL} values by a specific capacitance C_S of 0.04 mF cm^{-2} [35]. The overpotentials from the LSV curves normalized to the ECSA were obtained at a current density of 0.02 mA $cm^{-2}{}_{ECSA}$ (Figure 2c,f). Here, the ECSA normalization for the NFS−N_2 electrocatalysts results in clearly separated overpotentials for $NFS_{100}-N_2$ (329 ± 13 mV) and the $NFS_{150}-N_2$ (353 ± 21 mV) electrocatalysts, which have shown similar low non−Normalized overpotentials. A similar trend can be observed for $NFS_{250}-H_2$ and $NFS_{300}-H_2$ catalyzing the HER with overpotentials of 300 ± 9 mV and 272 ± 9 mV, respectively. Notably, $NFS_{100}-N_2$ catalyzes the HER at the lowest non−Normalized overpotential, while $NFS_{300}-H_2$ displays the lowest normalized overpotential. Thus, consideration of particle size effects on the

electrocatalytic activity is important to determine intrinsic material properties. In addition, we performed electrochemical impedance spectroscopy (EIS) measurements, which reveal similar trends compared to the non−Normalized LSV data (Figure S5). Here, $NFS_{150}-N_2$ and $NFS_{300}-H_2$ show the smallest Nyquist arcs of approx. 25 Ω, which increases to approx. 110 and 160 Ω for $NFS_{250}-N_2$ and $NFS_{150}-H_2$, respectively.

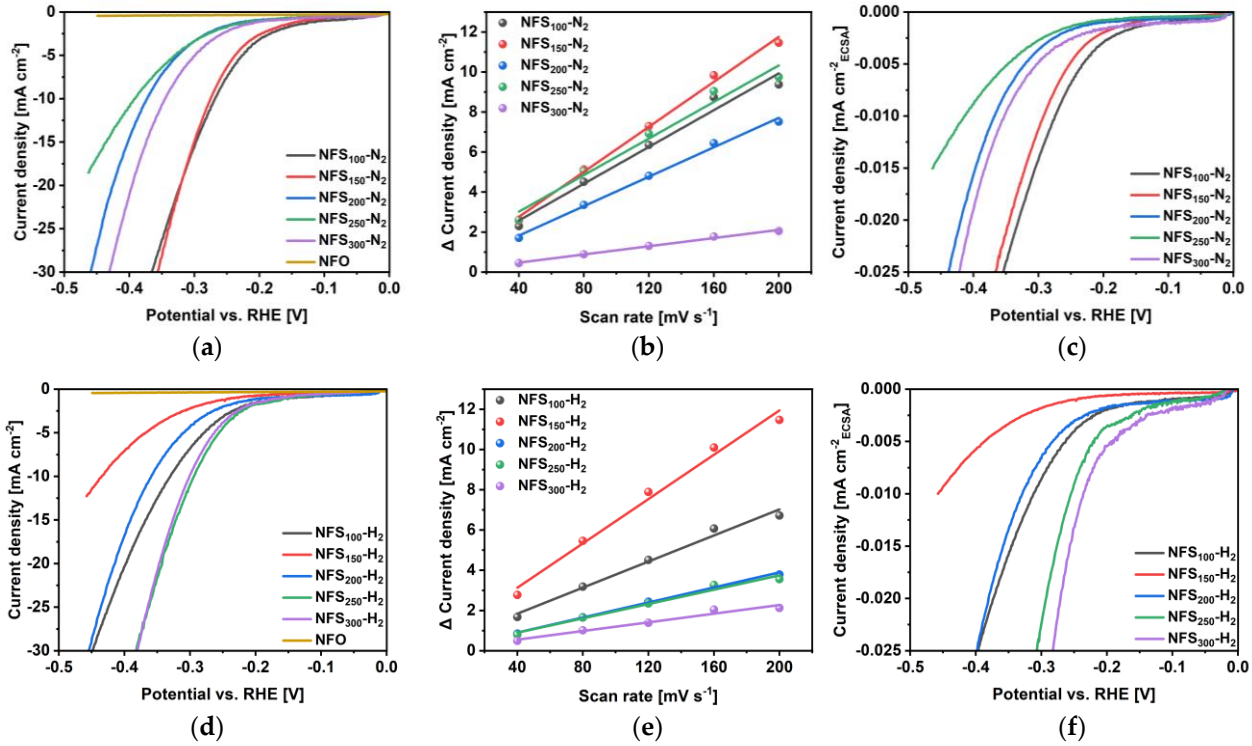

Figure 2. Electrochemical performance data of the $NFS-N_2$ electrocatalysts showing (**a**) non−Normalized LSV curves, (**b**) C_{DL} values obtained by cyclic voltammetry and (**c**) LSV curves normalized by the ECSA. Electrochemical performance data of the $NFS-H_2$ electrocatalysts showing (**d**) non−Normalized LSV curves, (**e**) C_{DL} values obtained by cyclic voltammetry and (**f**) LSV curves normalized by the ECSA.

To test the stability of the NFS electrocatalysts, we performed chronopotentiometry experiments for 1 h at a current density of −10 mA cm^{-2} (Figure 3a,b). A stable performance with a minor activation or deactivation behavior can be observed depending on the investigated electrocatalyst. For example, the NFO precursor catalyst shows the highest potential required to catalyze the HER and shows an activation behavior over the duration of the experiment. However, the overall activity after 1 h is inferior to the synthesized NFS materials. In comparison, most of the $NFS-N_2$ electrocatalysts, except for $NFS_{250}-N_2$, show a slight deactivation within 1 h. The deactivation behavior can also be observed for $NFS_{100}-H_2$ and $NFS_{200}-H_2$; however, a deactivation behavior from a particle detachment from the electrode cannot be generally excluded. Interestingly, $NFS_{250}-H_2$ and $NFS_{300}-H_2$, which catalyze the HER with the lowest potential, show a stable performance. We therefore subjected the $NFS_{300}-H_2$ electrocatalyst to an elongated electrolysis at −10 and −100 mA cm^{-2} for 10 h, respectively (Figure 3c). Here, the HER was also catalyzed with a stable performance by $NFS_{300}-H_2$.

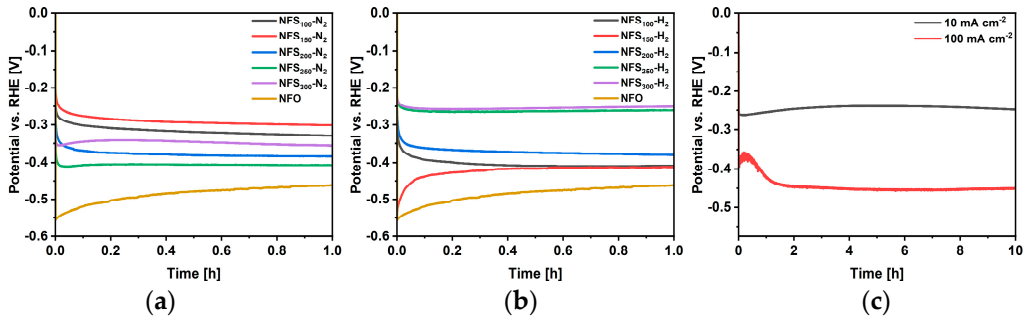

Figure 3. Chronopotentiometry data obtained from the (**a**) NFS−N_2 electrocatalysts at 10 mA cm^{-2}, (**b**) NFS−H_2 electrocatalysts at 10 mA cm^{-2} and (**c**) NFS_{300}−H_2 electrocatalyst at −10 and 100 mA cm^{-2} for 10 h.

It can be concluded that NiFe (oxy)sulfide materials catalyze the electrochemical HER with efficiencies depending on the S:M ratio and the materials phase. The NFS_{100}−N_2 and $NFS_{H2,300}$ °C show high overall activities; however, since the NFS−N_2 materials mostly tend to deactivate during catalysis, the usage of the fully sulfidized NFS_{300}−H_2 material should be prioritized, which displayed stability for 10 h at −100 mA cm^{-2}.

4. Conclusions

A series of bimetallic NiFe (oxy)sulfide materials was synthesized by heating the transition metal oxide NFO in H_2S-containing atmospheres. Depending on the choice of the H_2S gas composition and the applied reaction temperature, a control of the sulfur incorporation into NFO and the materials phase was achieved. For example, a sulfidation of NFO was observed at low temperatures of 100 °C and full conversion into the nickelian pyrite ($Ni_{0.30}Fe_{0.71}S_{1.99}$) and pyrrhotite ($Ni_{0.30}Fe_{0.64}S_{1.06}$) sulfide materials were realized at 300 °C. SEM analysis and the particle size analysis by the laser diffraction technique revealed a broad particle size distribution caused by the particle sintering of the NFS materials.

Furthermore, we assessed the electrochemical HER performance of the NFS materials in 1 M KOH. The electrochemical performance varied with the sulfur content and the materials phase. Materials with a S:M ratio of approx. 1 and/or a nickelian pyrrhotite phase catalyzed the HER with the lowest overpotentials of 266 ± 12 mV and 302 ± 9 mV vs. RHE at −10 mA cm^{-2} for NFS_{100}−N_2 and NFS_{250}−H_2, respectively. Additionally, a normalization of the geometric current density by the ECSA was performed, which revealed the lowest overpotential of 272 ± 9 mV vs. RHE at a current density of 0.02 mA $cm^{-2}{}_{ECSA}$ catalyzed by NFS_{300}−H_2. Here, NFS_{100}−N_2 and NFS_{300}−H_2 showed the lowest overpotential for the non−Normalized and the ECSA−Normalized LSV data, respectively. Therefore, particle size effects should be included in the consideration of the HER activity. Finally, preliminary stability measurements have revealed a rather deactivating behavior of NFS−N_2 materials, while the NFS_{300}−H_2 was able to catalyze the HER at current densities of −10 and −100 mA cm^{-2} with stable potentials for 10 h.

These results represent another step towards designing transition metal chalcogenide catalyst materials for the electrochemical HER and point the way towards the most efficient stoichiometric formulations of NiFe (oxy)sulfide-based catalysts.

Supplementary Materials: The following are available online at https://www.mdpi.com/article/10.3390/en15020543/s1, Figure S1: XPS data of the synthesized NFS materials. Figure S2: Deconvoluted XPS spectra of NFS_{300}−H_2. Figure S3: Deconvoluted XPS spectra of NFS_{100}−N_2. Figure S4: SEM images of the synthesized NFS−N_2 materials. Figure S5: SEM images of the synthesized NFS−H_2 materials. Figure S6: Representative SEM images at NFS_{100}−H_2 and NFS_{100}−N_2 at distinct magnifications. Figure S7: Particle size analysis by laser diffraction. Figure S8: Representative CV measurements for determination of C_{DL}. Figure S9: EIS spectra of the NFS materials. Figure S10: Tafel analysis of NFS materials.

Author Contributions: Conceptualization, D.T.; methodology, D.T.; validation, D.T. and V.A.; formal analysis, D.T. and V.A.; investigation, D.T. and V.A.; resources, D.T. and C.S.; data curation, D.T.; writing—original draft preparation D.T.; writing—review and editing, D.T., V.A., C.S., D.S., K.j.P., R.M. and U.-P.A.; visualization, D.T.; supervision, D.S., K.j.P. and U.-P.A.; funding acquisition, U.-P.A. All authors have read and agreed to the published version of the manuscript.

Funding: This research was funded by the German Research Foundation DFG (AP242/6–1, MA 5392/7–1). U.-P.A. is grateful for financial support from the Deutsche Forschungsgemeinschaft (under Germany's Excellence Strategy—EXC-2033—Project number 390677874), the Fraunhofer Internal Programs under Grant no. Attract 097–602175, and the Fraunhofer Cluster of Excellence CINES. Open access funding was enabled and organized by Projekt DEAL.

Institutional Review Board Statement: Not applicable.

Informed Consent Statement: Not applicable.

Data Availability Statement: Not applicable.

Acknowledgments: The authors gratefully acknowledge funding by the German Research Foundation DFG (AP242/6–1, MA 5392/7–1). U.-P.A. is grateful for financial support from the Deutsche Forschungsgemeinschaft (under Germany's Excellence Strategy—EXC-2033—Project number 390677874), the Fraunhofer Internal Programs under Grant no. Attract 097–602175, and the Fraunhofer Cluster of Excellence CINES. Open access funding was enabled and organized by Projekt DEAL. The authors thank Stephan Spöllmann (RUBION) for measuring XPS spectra.

Conflicts of Interest: The authors declare no conflict of interest.

References

1. Siegmund, D.; Metz, S.; Peinecke, V.; Warner, T.E.; Cremers, C.; Grevé, A.; Smolinka, T.; Segets, D.; Apfel, U.-P. Crossing the Valley of Death: From Fundamental to Applied Research in Electrolysis. *JACS Au* **2021**, *1*, 527–535. [CrossRef] [PubMed]
2. Chu, S.; Majumdar, A. Opportunities and challenges for a sustainable energy future. *Nature* **2012**, *488*, 294–303. [CrossRef] [PubMed]
3. Greeley, J.; Stephens, I.E.L.; Bondarenko, A.S.; Johansson, T.P.; Hansen, H.A.; Jaramillo, T.F.; Rossmeisl, J.; Chorkendorff, I.; Nørskov, J.K. Alloys of platinum and early transition metals as oxygen reduction electrocatalysts. *Nat. Chem.* **2009**, *1*, 552–556. [CrossRef] [PubMed]
4. Greeley, J.; Markovic, N.M. The road from animal electricity to green energy: Combining experiment and theory in electrocatalysis. *Energy Environ. Sci.* **2012**, *5*, 9246. [CrossRef]
5. Amer, M.S.; Ghanem, M.A.; Al-Mayouf, A.M.; Arunachalam, P.; Khdary, N.H. Low-loading of oxidized platinum nanoparticles into mesoporous titanium dioxide for effective and durable hydrogen evolution in acidic media. *Arab. J. Chem.* **2020**, *13*, 2257–2270. [CrossRef]
6. Boppella, R.; Tan, J.; Yun, J.; Manorama, S.V.; Moon, J. Anion-mediated transition metal electrocatalysts for efficient water electrolysis: Recent advances and future perspectives. *Coord. Chem.* **2021**, *427*, 213552. [CrossRef]
7. Hu, C.; Zhang, L.; Gong, J. Recent progress made in the mechanism comprehension and design of electrocatalysts for alkaline water splitting. *Energy Environ. Sci.* **2019**, *12*, 2620–2645. [CrossRef]
8. Li, A.; Sun, Y.; Yao, T.; Han, H. Earth-Abundant Transition-Metal-Based Electrocatalysts for Water Electrolysis to Produce Renewable Hydrogen. *Chem. Eur. J.* **2018**, *24*, 18334–18355. [CrossRef]
9. Li, Y.H.; Liu, P.F.; Pan, L.F.; Wang, H.F.; Yang, Z.Z.; Zheng, L.R.; Hu, P.; Zhao, H.J.; Gu, L.; Yang, H.G. Local atomic structure modulations activate metal oxide as electrocatalyst for hydrogen evolution in acidic water. *Nat. Commun.* **2015**, *6*, 8064. [CrossRef] [PubMed]
10. Li, L.; Zhang, T.; Yan, J.; Cai, X.; Liu, S.F. P Doped MoO_{3-x} Nanosheets as Efficient and Stable Electrocatalysts for Hydrogen Evolution. *Small* **2017**, *13*, 1700441. [CrossRef]
11. Zeng, H.; Chen, S.; Jin, Y.Q.; Li, J.; Song, J.; Le, Z.; Liang, G.; Zhang, H.; Xie, F.; Chen, J.; et al. Electron Density Modulation of Metallic MoO 2 by Ni Doping to Produce Excellent Hydrogen Evolution and Oxidation Activities in Acid. *ACS Energy Lett.* **2020**, *5*, 1908–1915. [CrossRef]
12. Zhu, Y.; Lin, Q.; Zhong, Y.; Tahini, H.A.; Shao, Z.; Wang, H. Metal oxide-based materials as an emerging family of hydrogen evolution electrocatalysts. *Energy Environ. Sci.* **2020**, *13*, 3361–3392. [CrossRef]
13. Guo, Y.; Park, T.; Yi, J.W.; Henzie, J.; Kim, J.; Wang, Z.; Jiang, B.; Bando, Y.; Sugahara, Y.; Tang, J.; et al. Nanoarchitectonics for Transition-Metal-Sulfide-Based Electrocatalysts for Water Splitting. *Adv. Mater.* **2019**, *31*, 1807134. [CrossRef] [PubMed]
14. Siegmund, D.; Blanc, N.; Smialkowski, M.; Tschulik, K.; Apfel, U.-P. Metal-Rich Chalcogenides for Electrocatalytic Hydrogen Evolution: Activity of Electrodes and Bulk Materials. *ChemElectroChem* **2020**, *7*, 1514–1527. [CrossRef]

15. Larquet, C.; Carenco, S. Metal Oxysulfides: From Bulk Compounds to Nanomaterials. *Front. Chem.* **2020**, *8*, 179. [CrossRef] [PubMed]
16. Nelson, A.; Fritz, K.E.; Honrao, S.; Hennig, R.G.; Robinson, R.D.; Suntivich, J. Increased activity in hydrogen evolution electrocatalysis for partial anionic substitution in cobalt oxysulfide nanoparticles. *J. Mater. Chem. A* **2016**, *4*, 2842–2848. [CrossRef]
17. Sarma, P.V.; Vineesh, T.V.; Kumar, R.; Sreepal, V.; Prasannachandran, R.; Singh, A.K.; Shaijumon, M.M. Nanostructured Tungsten Oxysulfide as an Efficient Electrocatalyst for Hydrogen Evolution Reaction. *ACS Catal.* **2020**, *10*, 6753–6762. [CrossRef]
18. Vignais, P.M.; Billoud, B. Occurrence, classification, and biological function of hydrogenases: An overview. *Chem. Rev.* **2007**, *107*, 4206–4272. [CrossRef]
19. Pandey, A.S.; Harris, T.V.; Giles, L.J.; Peters, J.W.; Szilagyi, R.K. Dithiomethylether as a ligand in the hydrogenase h-cluster. *J. Am. Chem. Soc.* **2008**, *130*, 4533–4540. [CrossRef]
20. Möller, F.; Piontek, S.; Miller, R.G.; Apfel, U.-P. From Enzymes to Functional Materials-Towards Activation of Small Molecules. *Chem. Eur. J.* **2018**, *24*, 1471–1493. [CrossRef]
21. Shang, X.; Chi, J.-Q.; Liu, Z.-Z.; Dong, B.; Yan, K.-L.; Gao, W.-K.; Zeng, J.-B.; Chai, Y.-M.; Liu, C.-G. Ternary Ni-Fe-V sulfides bundles on nickel foam as free-standing hydrogen evolution electrodes in alkaline medium. *Electrochim. Acta* **2017**, *256*, 241–251. [CrossRef]
22. McGlynn, S.E.; Kanik, I.; Russell, M.J. Peptide and RNA contributions to iron-sulphur chemical gardens as life's first inorganic compartments, catalysts, capacitors and condensers. *Phil. Trans. R. Soc. A* **2012**, *370*, 3007–3022. [CrossRef]
23. Konkena, B.; Junge Puring, K.; Sinev, I.; Piontek, S.; Khavryuchenko, O.; Dürholt, J.P.; Schmid, R.; Tüysüz, H.; Muhler, M.; Schuhmann, W.; et al. Pentlandite rocks as sustainable and stable efficient electrocatalysts for hydrogen generation. *Nat. Commun.* **2016**, *7*, 12269. [CrossRef]
24. Piontek, S.; Andronescu, C.; Zaichenko, A.; Konkena, B.; Junge Puring, K.; Marler, B.; Antoni, H.; Sinev, I.; Muhler, M.; Mollenhauer, D.; et al. Influence of the Fe:Ni Ratio and Reaction Temperature on the Efficiency of $(Fe_xNi_{1-x})_9S_8$ Electrocatalysts Applied in the Hydrogen Evolution Reaction. *ACS Catal.* **2018**, *8*, 987–996. [CrossRef]
25. Zhang, W.; Li, D.; Zhang, L.; She, X.; Yang, D. NiFe-based nanostructures on nickel foam as highly efficiently electrocatalysts for oxygen and hydrogen evolution reactions. *J. Energy Chem.* **2019**, *39*, 39–53. [CrossRef]
26. Wang, X.; Zong, X.; Liu, B.; Long, G.; Wang, A.; Xu, Z.; Song, R.; Ma, W.; Wang, H.; Li, C. Boosting Electrochemical Water Oxidation on NiFe (oxy) Hydroxides by Constructing Schottky Junction toward Water Electrolysis under Industrial Conditions. *Small* **2021**, *7*, e2105544. [CrossRef] [PubMed]
27. Zhang, Z.; Wu, Y.; Zhang, D. Potentiostatic electrodeposition of cost-effective and efficient Ni–Fe electrocatalysts on Ni foam for the alkaline hydrogen evolution reaction. *Int. J. Hydrogen Energy* **2021**, *47*, 1425–1434. [CrossRef]
28. Li, B.-Q.; Zhang, S.-Y.; Tang, C.; Cui, X.; Zhang, Q. Anionic Regulated NiFe (Oxy)Sulfide Electrocatalysts for Water Oxidation. *Small* **2017**, *13*, 1700610. [CrossRef]
29. Liu, J.; Zhu, D.; Ling, T.; Vasileff, A.; Qiao, S.Z. Anthony Vasileff; Shi-Zhang Qiao. S−NiFe2O4 ultra-small nanoparticle built nanosheets for efficient water splitting in alkaline and neutral pH. *Nano Energy* **2017**, *40*, 264–273. [CrossRef]
30. Simon, C.; Zakaria, M.B.; Kurz, H.; Tetzlaff, D.; Blösser, A.; Weiss, M.; Timm, J.; Weber, B.; Apfel, U.-P.; Marschall, R. Magnetic $NiFe_2O_4$ Nanoparticles Prepared via Non-Aqueous Microwave-Assisted Synthesis for Application in Electrocatalytic Water Oxidation. *Chem. Eur. J.* **2021**, *27*, 16990–17001. [CrossRef]
31. Bezverkhyy, I.; Danot, M.; Afanasiev, P. New Low-Temperature Preparations of Some Simple and Mixed Co and Ni Dispersed Sulfides and Their Chemical Behavior in Reducing Atmosphere. *Inorg. Chem.* **2003**, *42*, 1764–1768. [CrossRef] [PubMed]
32. Wyckoff, R.W.G. The structure of crystals. *J. Chem. Technol. Biotechnol.* **1931**, *50*, 877. [CrossRef]
33. Alsén, N. Röntgenographische Untersuchung der Kristallstrukturen von Magnetkies, Breithauptit, Pentlandit, Millerit und verwandten Verbindungen. *Geol. Fören. Stock. Förh.* **1925**, *47*, 19–72. [CrossRef]
34. Baylis, P. Crystal structure refinement of a weakly anisotropic pyrite. *Am. Mineral.* **1977**, *62*, 1168–1172.
35. McCrory, C.C.L.; Jung, S.; Ferrer, I.M.; Chatman, S.M.; Peters, J.C.; Jaramillo, T.F. Benchmarking hydrogen evolving reaction and oxygen evolving reaction electrocatalysts for solar water splitting devices. *J. Am. Chem. Soc.* **2015**, *137*, 4347–4357. [CrossRef] [PubMed]